

Article

Numerical Analysis of Flow Boiling Characteristics of a Single Channel Heat Sink Subjected to Multiple Heat Sources

Jiyu Qian ¹, Rui Wang ¹, Tao Wei ¹, Hao Tang ² and Dinghua Hu ^{2,*}¹ Nanjing Research Institute of Electronics Technology, Nanjing 210094, China² MIIT Key Laboratory of Thermal Control of Electronic Equipment, School of Energy and Power Engineering, Nanjing University of Science and Technology, Nanjing 210094, China

* Correspondence: dhhu@njust.edu.cn

Abstract: High-power electronic devices with multiple heat sources often require temperature uniformity and to operate within their functional temperature range for optimal performance. Micro-channel cooling could satisfy the heat dissipation requirements, but it may cause temperature non-uniformity. In this paper, simulations are performed for different geometric parameters of the channel and the position of the heat source. The results show that a flattened channel can effectively reduce the heat source temperature, broadening the straight channel can reduce the flow resistance and enhance heat transfer, while widening the channel at the bend may lead to local dryness. Meanwhile, a thermal model is established to analyze the influence of the position of the heat source. The results also show that with the increase in the curved channel radius, the phenomenon of vapor-liquid separation becomes more obvious, the pressure drop decreases, but the heat transfer effect worsens.

Keywords: numerical simulations; heat transfer enhancement; performance analysis; two-phase flow



Citation: Qian, J.; Wang, R.; Wei, T.; Tang, H.; Hu, D. Numerical Analysis of Flow Boiling Characteristics of a Single Channel Heat Sink Subjected to Multiple Heat Sources. *Energies* **2023**, *16*, 3060. <https://doi.org/10.3390/en16073060>

Academic Editor: Kyung Chun Kim

Received: 24 February 2023

Revised: 22 March 2023

Accepted: 24 March 2023

Published: 27 March 2023



Copyright: © 2023 by the authors. Licensee MDPI, Basel, Switzerland. This article is an open access article distributed under the terms and conditions of the Creative Commons Attribution (CC BY) license (<https://creativecommons.org/licenses/by/4.0/>).

1. Introduction

The miniaturization and increased integration of multi-chip electronic devices causes high heat flux [1,2]. The main purpose of thermal management is to decrease the temperature and/or temperature distribution. Micro-channel cooling is a promising technique that could satisfy the heat dissipation requirements, but large increases in the temperature of the refrigerant along the direction of flow could affect the temperature uniformity of multiple electronic devices [3]. Researchers often solve the problem by improving the heat source layout, designing the channel structure, and optimizing the channel layout [4,5].

Cho [6] designed micro-channels for nine chips distributed in a 3×3 array and optimized the micro-channel fins from a flat structure to a wedge structure with a gradually changing width. These two micro-channels are used to dissipate heat for nine chips, respectively. The research shows that a wedge channel structure with a gradually changing width has better temperature uniformity.

Kim et al. [7] investigated the thermal management of liquid-cooled cooling plates for multiple heat sources. Two array types of cooling plates to cool multiple heat sources scattered inside a humanoid robot are compared and analyzed according to total thermal resistance, total heat transfer rate, and surface temperature increases from a heating block to six multiple cooling plates. The results indicate that two-way parallel circulation shows better thermal performance in all cases.

Mao et al. [8] established a compact thermal model for a micro-channel with high temperature uniformity subjected to multiple heat sources. The compact thermal model is used to optimize the geometrical structure of a fractal tree-like micro-channel substrate to achieve temperature uniformity of the heat sources. Ma et al. [9] conducted a thermal analysis and modeling of an LED array integrated as a liquid cooling module. Yuan et al. [10] analyzed the thermal performance of a high-power LED array with a microchannel cooler. Tan et al. [11] designed three micro-channel topologies for a multi-heat source-phased

array antenna, and improved the micro-channel structure with the aim of temperature equalization among multiple heat sources. A T-shaped longitudinal microchannel structure has the best temperature uniformity when the heat source power is high.

Other micro-channel shapes and configurations, such as H-type bifurcation structure [12], density-based topology optimization [13], fractal tree-like structures [14], hierarchical manifolds [15], and spider web-like structures [16], have also been proposed to satisfy the heat dissipation and temperature uniformity requirements. The optimization of the micro-channel structures is a passive enhancement; some researchers also adopt the active control method. Bo et al. [17] propose a combined solution for the heat dissipation of multi-chip devices by independently controlling multiple thermoelectric cooler currents. Laguna et al. [18] propose a cooling array with self-adaptive micro-valves to improve the temperature uniformity of chips and reduce the pumping power. Li et al. [19] propose a self-adaptive micro-channel cooling system with a thermal-sensitive nanocomposite hydrogel to intelligently adjust the coolant. The details of these studies are shown in Table 1.

Table 1. Results of previous studies investigating the solution to heat dissipation and temperature uniformity for multiple heat sources.

| Study | Improvement Result |
|---|--|
| H-type bifurcation structure [12] | The average temperature deviation is less than ± 5 K. |
| density-based topology optimization [13] | The highest temperature and average temperature are both decreased by 10 °C while the pressure drop is unchanged. |
| fractal tree-like structures [14] | The maximum temperature difference among the heat sources is 1.3 K. |
| hierarchical manifolds [15] | The heat sink with $15 \mu\text{m} \times 300 \mu\text{m}$ channels is shown to dissipate base heat fluxes up to 910 W/cm^2 at pressure drops of less than 1.62 bar. |
| spider web-like structures [16] | The optimal structure can meet the requirements of temperature uniformity within 2 K at a higher heat flux of 150 W/cm^2 . |
| a combined solution of thermoelectric coolers and micro-channels [17] | It can achieve precise temperature control of multiple chips with maximum temperature difference less than 0.3 K and temperature standard deviation less than 0.07 K when the heat flux is 50 W/cm^2 . |
| a cooling array with self-adaptive micro valves [18] | The tailored micro-channel device reaches a temperature uniformity of 4 K with a pumping power lower than 0.001% of the chip power. |
| self-adaptive chip cooling with template-fabricated nanocomposite hydrogel [19] | A heat flux of 100 W/cm^2 can be extracted with a similar increase in temperature, while the coefficient of performance (COP) is improved by an order of magnitude. |

In the present research, the heat sink with a single channel is preferred because single channels exhibit better flow boiling stability compared with multiple channels [20], so it is particularly critical to design the channel layout. The primary objective of this work is to better understand the effect of the geometric parameters of the channel and the position of the heat source on the performance of heat transfer, in order to optimize the design of a cooling plate channel subjected to multiple heat sources. From the review, most of the literature discussed the multi-channel optimization for multi heat sources, while this study focuses on the single channel for multiple heat sources, which is usually encountered in actual cases. This study could provide a reference for the channel design of a cooling plate.

Numerical simulations are performed for different geometric parameters of the channel and the radius of the curved channel. The effect of the position of the heat source is also studied in detail.

2. Calculation Method

2.1. Physical Model

Figure 1a shows the structure of the heat sink; the total size is $170\text{ mm} \times 170\text{ mm}$. It is composed of (1) 16 discrete heat sources with dimensions of $10\text{ mm} \times 10\text{ mm} \times 3\text{ mm}$, each with a heating power of 125 W ; (2) 16 thermal expansion boards with dimensions of $13\text{ mm} \times 35\text{ mm} \times 2\text{ mm}$ just below the heat sources; and (3) a cooling plate with assembly holes and its cover plate. The flow channel is set in the substrate. The section is shown as Figure 1b.

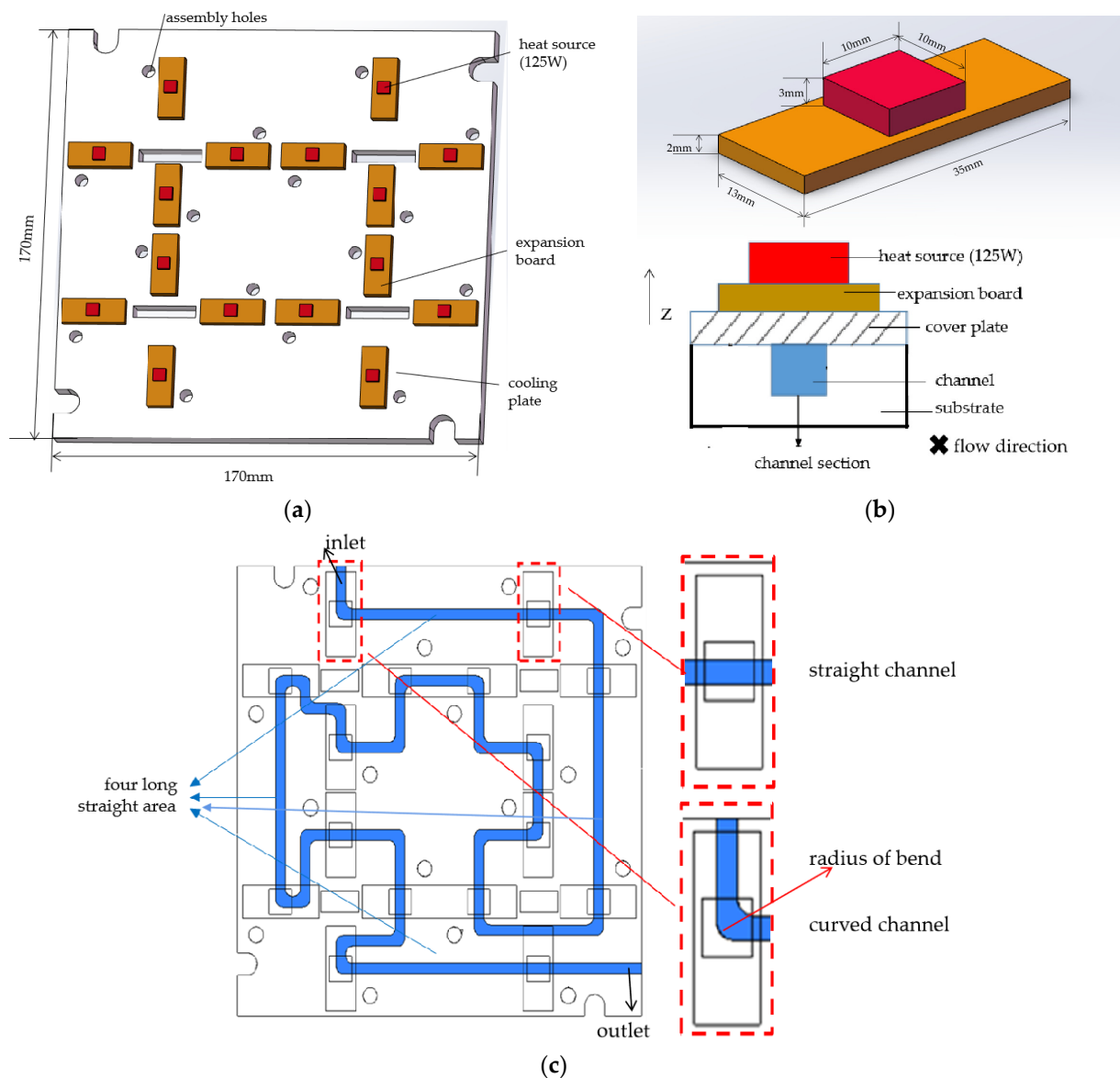


Figure 1. Schematic diagram of: (a) heat sink; (b) section of heat sink; (c) channel.

R134a is selected as the refrigerant flowing in the channel. Compared with single-phase flow, two-phase flow forced convection boiling could better satisfy the heat dissipation requirements. To ensure the heat transfer effect, the channel is set just below the heat sources and is already designed for temperature uniformity. The channel is shown as

the blue line in Figure 1c. The temperature of the working fluid increases along the flow direction; therefore, the temperature of the downstream heater is much higher than that of the upstream heater. The channel in this study is designed to flow through the last few heaters first to reduce the temperature of the downstream heater, in order to improve the temperature uniformity.

As shown in Figure 1b, the main heat exchange area of the heat sink lies in the area from the lower surface of the heat source to the upper surface of the channel. The superior height of the channel makes it hard to make full use of the refrigerant at the bottom, so increasing the area of the upper surface of the channel can improve the heat exchange effect. Therefore, keeping the channel size in the non-heat area and the distance from the upper surface of the channel to the upper surface of heat sink unchanged, the channel will be increasingly flat as the channel width increases. A tangent arc is produced to make the interface change smoother, reduce the pressure drop, avoid the local liquid phase and vapor stagnation zone, and prevent the local heat transfer from deteriorating. The schematic diagram of the channel with variable cross-section is shown in Figure 2. Figure 2b shows the dimensions of the channel. In the present study, five designs are prepared; the width and height of the channels are 4 mm × 3 mm, 5 mm × 2.4 mm, 6 mm × 2 mm, 7 mm × 1.714 mm, and 8 mm × 1.5 mm, respectively. The R_1 of the 4 channel designs after broadening are 2.25 mm, 3.73 mm, 4.80 mm, and 5.60 mm, respectively, and the R_2 of the 4 channel designs after broadening are 1.61 mm, 3.31 mm, 5.02 mm, and 6.73 mm, respectively.

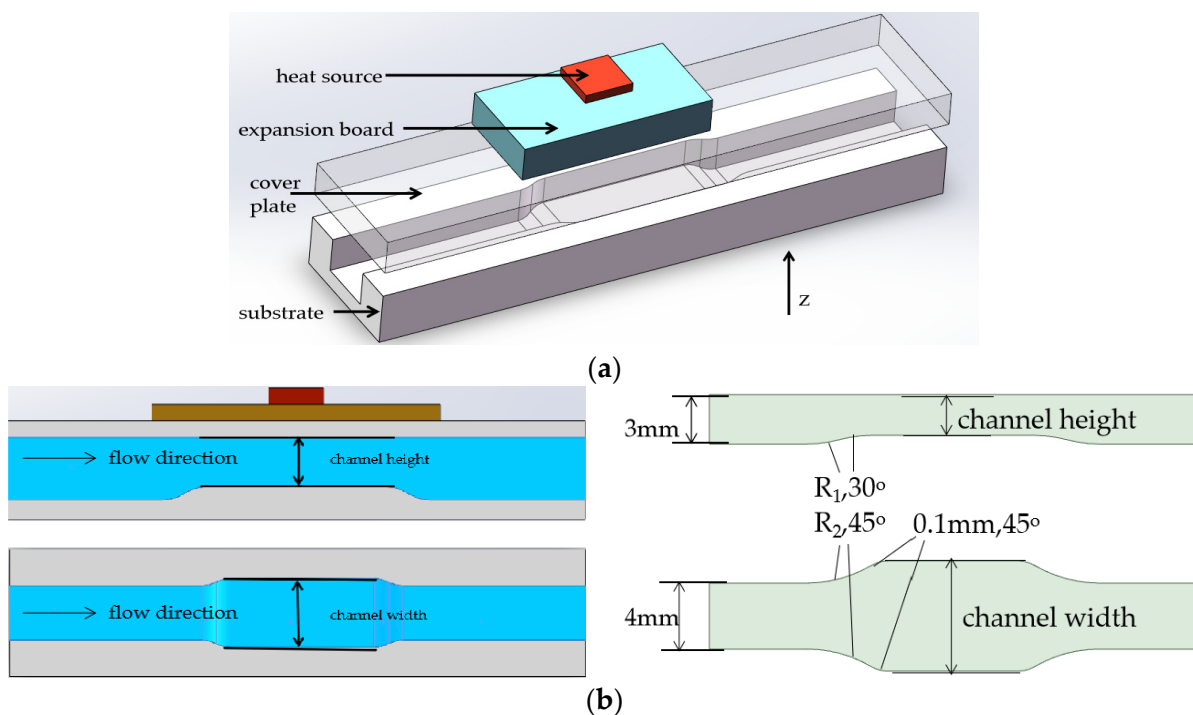


Figure 2. Schematic diagram of (a) structure of channel with variable cross-section; (b) channel section and dimensions.

As shown in Figure 1c, there are 23 bends in the single channel, which forms four long straight areas. The channel section of these four straight areas is an important geometric parameter for the flow boiling characteristics of heat sink. Therefore, it is necessary to design the channel after broadening. Figure 3b shows the broadened channel. Compared with the original channel (Figure 3a), there is no difference except that the four straight channels are wider.

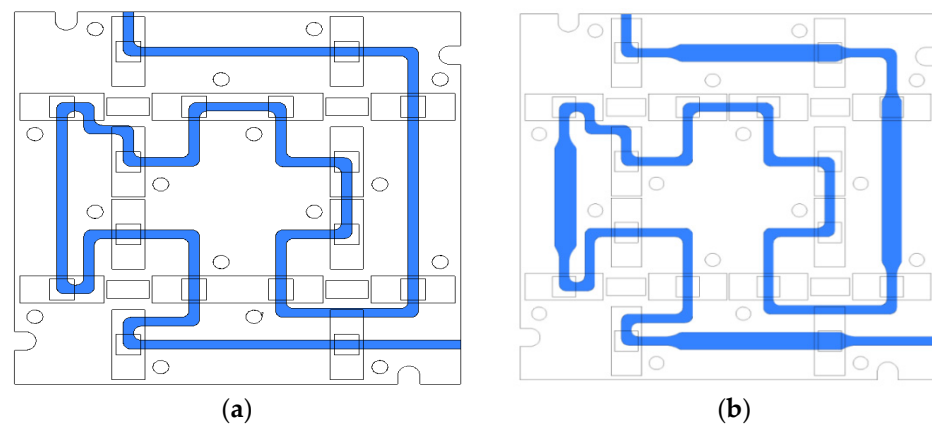


Figure 3. Schematic diagram of expansion of straight channel. (a) Original channel; (b) broadened channel.

Figure 1c also shows that the channel structure at the bottom of the heat source exhibits two typical characteristics: straight channel and curved channel. The 16 heat sources have different positional relationships with the closest bend: the heat source is placed in front of the bend, near the bend, just above the bend, or behind the bend. The models shown in Figure 4 are designed for the purpose of comparison.

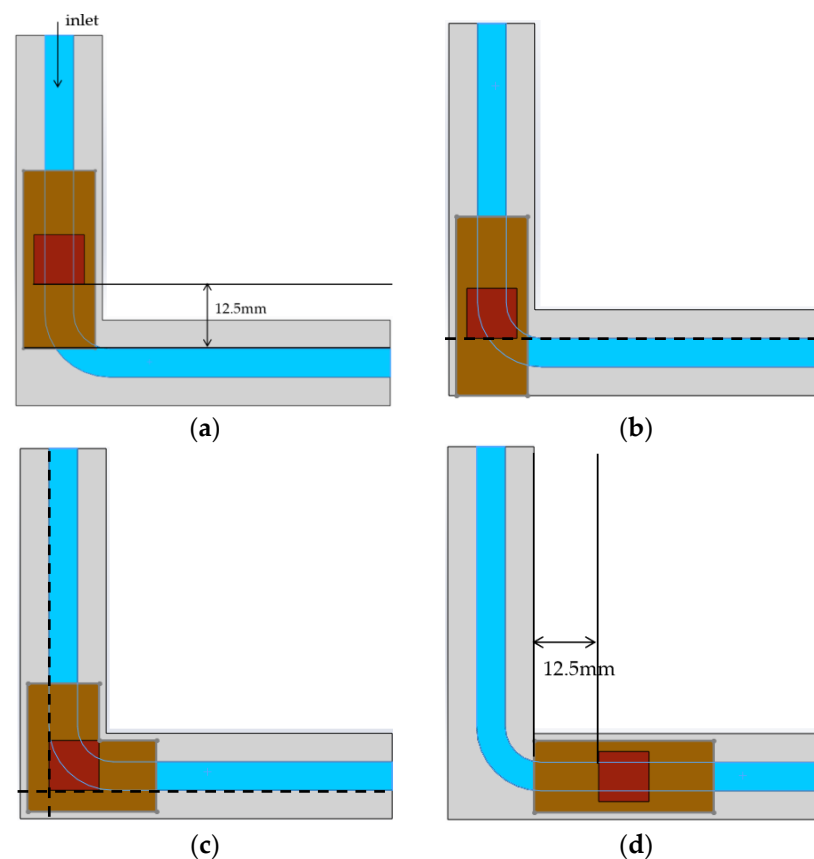


Figure 4. Schematic diagram of positional relationships between heat source and bend: (a) in front of the bend; (b) near the bend; (c) just above the bend; (d) behind the bend.

2.2. Mathematical Models

A suitable multi-phase model is crucial to accurately obtain correct simulation results in flow boiling. The Volume of Fluid (VOF), Mixture and Eulerian models are widely applied in multi-phase simulation. Using the VOF model, it is easy to capture vapor–liquid

interface and bubbles, but its simulation accuracy in the temperature field is unsatisfactory, so VOF is only used to simulate bubble activity in the relevant research. The Mixture model has good convergence, but its accuracy and capacity to capture the vapor–liquid interface are poor. The Eulerian model is the most complex multi-phase flow model. RPI model in the Eulerian model is well matched with the boiling heat transfer mechanism. Adopting the Eulerian model for steady-state calculation can not only obtain correct simulation results, but also reflect the two-phase flow in the channel by phase volume fraction. Thus, the Eulerian model is adopted in the present research.

In order to establish a reasonable and simplified simulation model, the following assumptions are adopted:

- (1) The mass flow rate is steady.
- (2) All energy lost by the bubble due to drag is converted to turbulence kinetic energy of the liquid in the wake of the bubble.
- (3) The outer surfaces of the model are all adiabatic.

The fluid flow and heat exchange in the heat sink are analyzed using the ANSYS Academic Research CFD. Equations (1)–(6) [21,22] show the governing equations solved in the present CFD model.

Mass equation of phase q :

$$\frac{\partial}{\partial t}(\alpha_q \rho_q) + \nabla(\alpha_q \rho_q v_q) = \sum_{p=1}^n (m_{pq} - m_{qp}) + S_q \quad (1)$$

where α_q and ρ_q represent the volume fraction and density of phase q , v_q represents the velocity vector, m_{pq} represents the mass transferred from phase p to phase q , m_{qp} represents the mass transferred from phase q to phase p , S_q represents the source item, $n \geq 2$.

Energy equation of phase q :

$$\begin{aligned} & \frac{\partial}{\partial t}(\alpha_q \rho_q h_q) + \nabla(\alpha_q \rho_q u_q h_q) \\ & = \alpha_q \frac{\partial p_q}{\partial t} + \tau_\sigma \nabla u_q - \nabla q_q + S_q + \sum_{p=1}^n (Q_{pq} + m_{pq} h_{pq} - m_{qp} h_{qp}) \end{aligned} \quad (2)$$

where h_q represents the enthalpy of phase q , q_q represents the heat flux, Q_{pq} represents the thermal transfer intensity of two phases, h_{pq} represents the enthalpy difference caused by the transformation of the phase p to the phase q , h_{qp} represents the enthalpy difference caused by the transformation of the phase q to the phase p .

Momentum equation of phase q :

$$\begin{aligned} & \frac{\partial}{\partial t}(\alpha_q \rho_q v_q) + \nabla(\alpha_q \rho_q v_q) \\ & = -\alpha_q \nabla p + \nabla \tau_q + \alpha_q \rho_q g + \sum_{p=1}^n (R_{pq} + m_{pq} v_{Aq} - m_{qp} v_{qp}) \\ & \quad + (F_q + F_{lift,q} + F_{wl,q} + F_{vm,q} + F_{td,q}) \end{aligned} \quad (3)$$

where τ_q represents the strain tensor of phase q ; F_q , $F_{lift,q}$, $F_{wl,q}$, $F_{vm,q}$, and $F_{td,q}$ represent external volume force, buoyancy, wall infiltration force, virtual mass force, interface force, and turbulent dispersion force of the phase q , respectively.

The pressure loss of refrigerant in the channel is mainly divided into the resistance loss along the way caused by viscous force and the local pressure loss at the bend caused by the change of channel direction.

Equation of pressure drop along the way:

$$\Delta p_1 = \lambda \frac{l}{D} \times \frac{\rho U^2}{2} \quad (4)$$

where λ represents the along-way resistance coefficient related to the roughness of the channel surface, l represents the length of the channel, D represents the hydraulic diam-

eter, ρ represents the density of the refrigerant, U represents the average flow rate of the refrigerant in the channel.

Equation of local pressure loss:

$$\Delta p_2 = \zeta \frac{\rho U^2}{2} \quad (5)$$

where ζ represents the local resistance coefficient. In this paper, all the bends of the channel are 90° , so the local resistance coefficient can also be calculated as:

$$\zeta = 0.13 + 1.85(D/2R)^{3.5} \quad (6)$$

where D represents the hydraulic diameter, R represents the bend radius of the channel.

The most common and known model for the numerical simulation of boiling is the RPI wall boiling model [23]. According to the RPI model, the total heat flux from the wall to the fluid is divided into three parts: q_C is the liquid-phase heat flux caused by the vicinity of the wall, q_Q is the quenching heat flux related to the convection of bubbles, and q_E is the evaporation heat flux:

$$q_w = q_C + q_Q + q_E \quad (7)$$

The convection of heat flux:

$$q_C = h_C(T_w - T_1)(1 - A_b) \quad (8)$$

where h_C is the convection heat transfer coefficient of liquid phase; T_w and T_1 are the wall temperature and fluid temperature neighbor to the wall, respectively; A_b is the wall surface to the area covered by the bubble.

q_Q , part of the total heat flux, which is periodically filled with T period by the liquid after separating the bubble from the surface, is given as:

$$q_Q = \frac{2k_l}{\sqrt{\pi\lambda_1 T}}(T_w - T_1) \quad (9)$$

where k_l is the thermal conductivity of liquid phase, λ_1 is the rate of diffusion, T is the period of time.

The evaporation heat flux is calculated from the following equations:

$$q_E = V_d N_w \rho_v h_{fv} f \quad (10)$$

where V_d is the volume of the bubble, N_w is the active nuclear density, ρ_v is the vapor density, h_{fv} is the evaporation latent heat, and f is the bubble departure frequency.

2.3. Numerical Method and Boundary Conditions

The finite volume-based technique is used for numerical modeling. Three-dimensional calculation is carried out by a double-precision solver. The first-order-upwind scheme is adopted for the discretization of the governing equations. The pressure and velocity are coupled using the couple algorithm. For the modeling of turbulence in flow boiling, the k-epsilon 2 eqn model is adopted. The calculated Coulomb number is set to 5. To improve the calculation accuracy, the Warped-Face Gradient Correction algorithm is activated. The iteration stops if the convergence criterion for the residual error is satisfied, which is $x_n - x_{n-1} < 10^{-5}$. x presents continuity, velocity, v_{f-vap} , energy, k , and epsilon.

At the inlet, the constant mass flow rate is 0.028512 kg/s, and the constant temperature of super-cooled fluid is 313.15 K. The pressure outlet boundary condition, i.e., the prescribed constant pressure, is applied to the outlet where saturation conditions are assumed for backflow. A constant volume heat of 125 W is prescribed in every heat source. At the

liquid–solid interface, a no-slip condition is applied for liquid, and the temperature and heat flux are continuous:

$$\begin{aligned} u_l &= 0 \\ T_l &= T_s \\ -k_l \frac{\partial T_l}{\partial n} &= -k_s \frac{\partial T_s}{\partial n} \end{aligned} \quad (11)$$

where the subscripts l and s denote liquid and solid, respectively.

2.4. Grid Generation and Independence Verification

Based on the ANSYS Meshing module, the models in this paper are meshed, and the tetrahedral and hexahedral grids are mixed. Mesh is refined where local velocity gradient and temperature gradient are large. The grid model is shown in Figure 5.

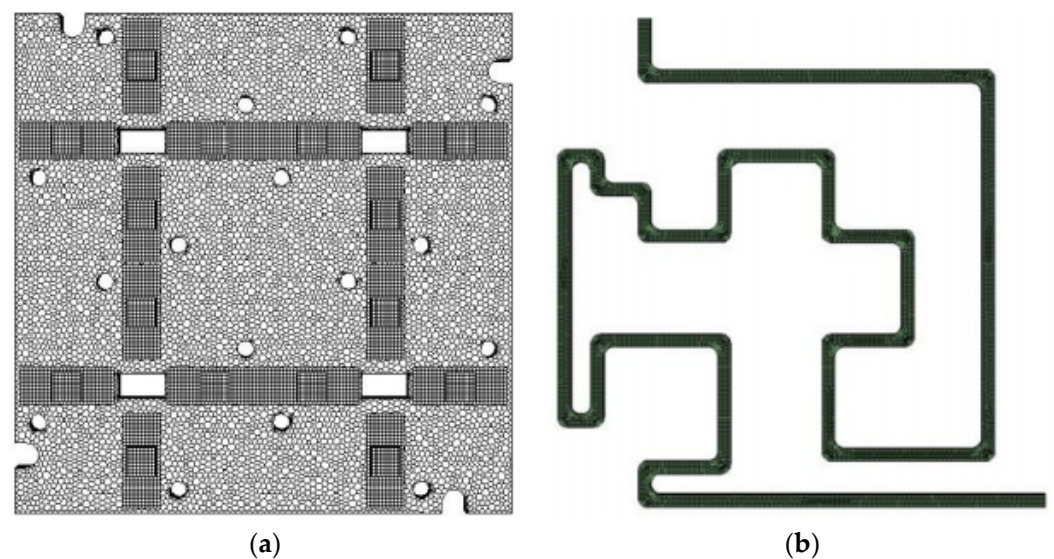


Figure 5. The grid model of (a) solid domain; (b) fluid domain.

The grid independence is studied under the different number of grids. Table 2 shows the variation of the temperature under a different number of grids. The grid independence verification was carried out showing convergence as a function of mesh refinement, with a final account of 603,921 grids with an error lower than 0.1% on heat source temperature compared with a mesh with 830,553 grids. For a single heat source and expansion board, the total number of elements is 2166 and 6992, respectively.

Table 2. The relation between temperature with typical element size and number of grids.

| Typical Element Size/mm | Number of Grids | T_w/K | α |
|-------------------------|-----------------|---------|----------|
| 1 | 158,418 | 333.82 | 0.74% |
| 0.8 | 247,298 | 335.25 | 0.31% |
| 0.5 | 429,389 | 336.00 | 0.09% |
| 0.1 | 830,553 | 336.31 | - |

3. Results and Discussion

3.1. Temperature and Vapor-Phase Distribution

Figure 6 shows the temperature distribution of the heat sources and vapor-phase distribution of the channel along the flow direction. Figure 7 shows that the vapor separation occurs at the bend. This was verified in previous experiments carried out by Nan, which can well verify the simulation results in this paper.

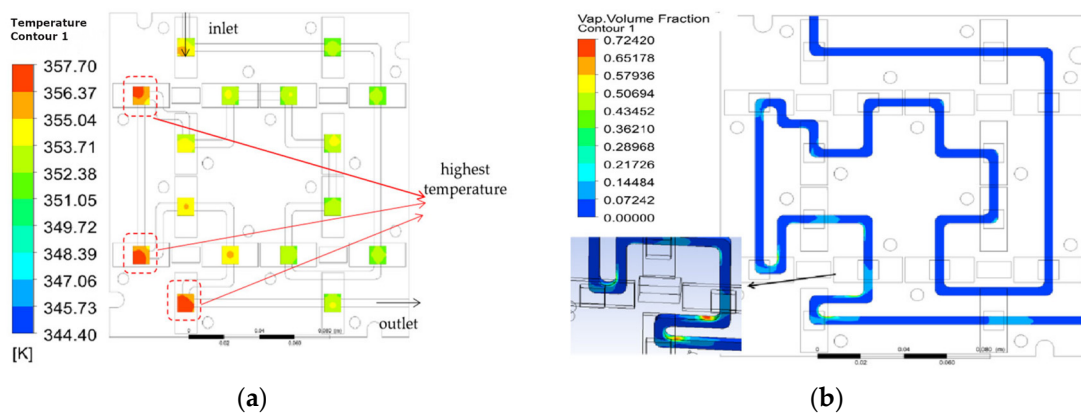


Figure 6. (a) Temperature distribution of heat sources; (b) vapor-phase distribution of the channel.

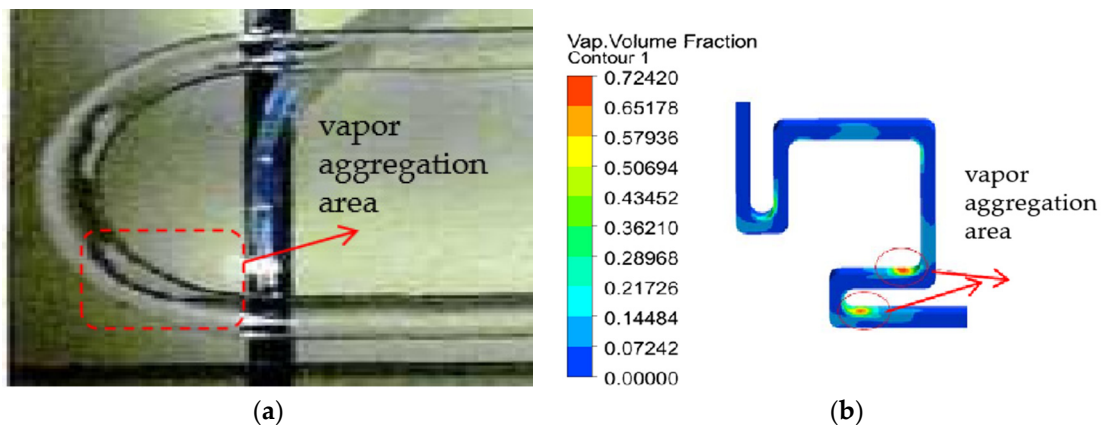


Figure 7. Vapor-liquid separation at the bend. (a) Nan's experimental result [24]; (b) numerical result.

As can be seen from Figure 6a, the temperature of the heat sources along the flow direction increases, but the three heat sources marked in the figure are contrary to this trend. It is not difficult to find that the three heat sources all take a continuous corner position, that is, there are more than two bends near the heat source.

Figure 6b shows that vapor separation occurs at the corners; there is a great difference in vapor volume fraction between the inside of the corner and the outside of the corner. The phenomenon of vapor separation is discussed in detail in Section 3.2.

As mentioned earlier, better understanding the effects of the geometric parameters of the channel and the position of the heat source on the flow boiling characteristics is the primary objective of this work. Therefore, simulations are performed with different geometric parameters and positions of the heat source.

3.2. Effect of Channel Section on Heat Transfer Performance and Pressure Drop Characteristics

Figure 8 shows that the difference of vapor-phase fraction between the upper and lower layers of the channel decreases as the channel width increases, which means the fluid in the channel is better-mixed. The part circled by the red circle is where the maximum vapor-phase fraction occurs. The maximum vapor-phase fraction of the straight channel occurs in the later part of the heat source (Figure 8a), while it occurs in the tapered part of the broadened channel (Figure 8b). This could be explained by the vapor separation. As shown in Figure 2b, the channel width is changed, and local fillet treatment is made by a tangent arc. For the channel after broadening, when the two-phase flow passes through the tangent arc, under the action of centrifugal force, the liquid preferentially rushes to the outside of the arc, forming a liquid phase gathering area. On the contrary, the vapor is

squeezed into the inside of the arc due to its smaller density and faster flow rate, resulting in the difference of vapor-phase distribution.

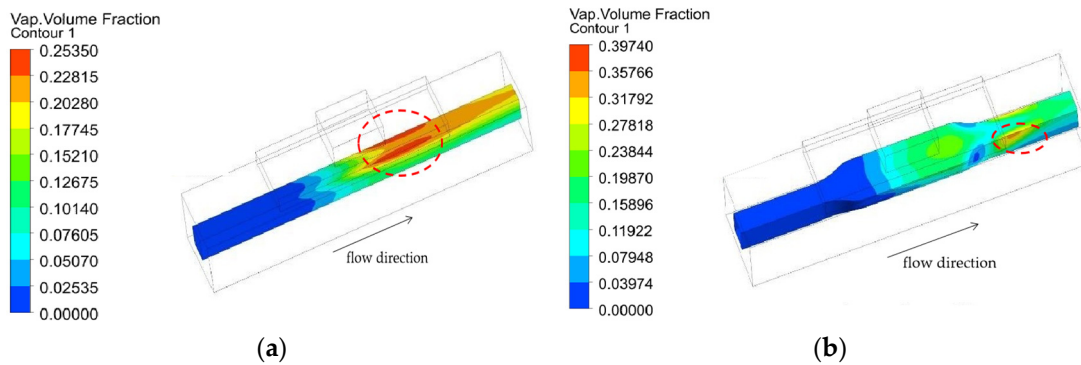


Figure 8. Vapor-phase distribution of different channel sections: (a) 4 mm × 3 mm; (b) 8 mm × 1.5 mm. The part circled by the red circle is where the maximum vapor-phase fraction occurs.

Table 3 and Figure 9 show that with the increase in channel width, the maximum temperature of the heat source decreases and the pressure drop increases gradually, which means the flat channel can effectively reduce the heat source temperature. Compared with the original channel, the 8 mm × 1.5 mm channel can reduce the temperature of the heat source by more than 2 K. This is because with the decrease in the height of the channel, the better-mixed fluid can improve the heat exchange capacity of the heat sink.

Table 3. Simulation results of different channel size.

| Channel Size | Highest Temperature of Heat Source/K | Average Temperature of Heat Source/K | Pressure Drop/Pa |
|-----------------|--------------------------------------|--------------------------------------|------------------|
| 4 mm × 3 mm | 367.34 | 365.32 | 1548.4 |
| 5 mm × 2.4 mm | 366.49 | 364.47 | 1593.9 |
| 6 mm × 2 mm | 366.19 | 364.14 | 1662.5 |
| 7 mm × 1.714 mm | 365.62 | 363.56 | 1702.4 |
| 8 mm × 1.5 mm | 365.13 | 363.05 | 1836.5 |

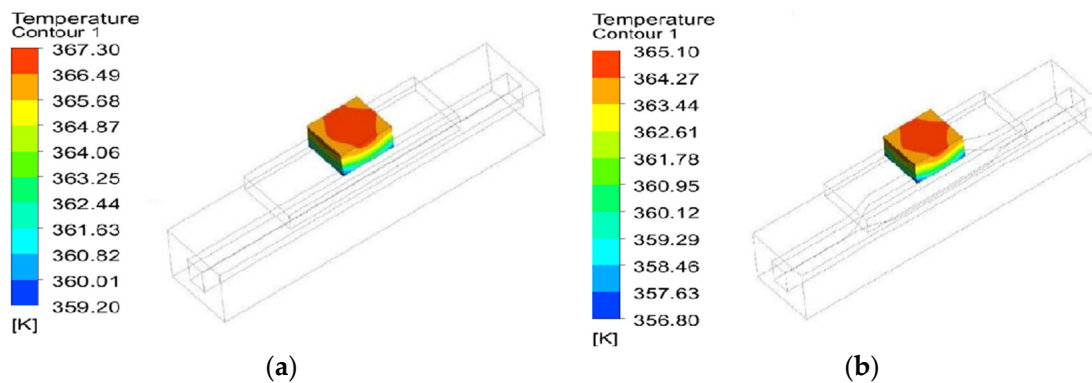


Figure 9. Temperature distribution of different channel sections: (a) 4 mm × 3 mm; (b) 8 mm × 1.5 mm.

In addition, the heat exchange area of the broadened channel increases, which strengthens the heat exchange effect with the heat source and improves the overall heat exchange capacity. Moreover, the change of the structure provides disturbance to the flow of refrigerant in the channel, which is also an important reason for the improvement of heat transfer performance.

However, the pressure drop increases due to the diffusion and contraction of the fluid in the up–down and left–right directions. It is worth mentioning that the pressure drop of a single structure is below 400 Pa, and no vapor gathers under the heat source due to the widening of the channel, so it can be suggested that the improved channel could improve the performance of heat sink.

3.3. Effect of Channel Expansion on Heat Transfer Performance and Pressure Drop Characteristics

Table 4 shows that the heat source temperature drops by about 9 K after expanding the channel width of the long straight area to 8 mm, and the heat transfer enhancement is remarkable. This is because the non-heat source area of the heat sink also plays a great role in the heat transfer effect. In the expanded channel area, the flow rate of fluid decreases, and the heat transfer with the plate surface is more sufficient. Moreover, there is a process of gradual contraction and expansion in each area, which creates a disturbance. For the later part of two-phase flow, this disturbance also enhances vapor–liquid mixing. At the same time, the expansion of the channel reduces the pressure drop along the widened part. Compared with the initial channel, the pressure drops of the channel widened to 6 mm and 8 mm decrease by 5300 Pa and 15,900 Pa, respectively.

Table 4. Numerical results of different channel width.

| Channel Width | Highest Temperature of Heat Source/K | Average Temperature of Heat Source/K | Pressure Drop/Pa |
|---------------|--------------------------------------|--------------------------------------|------------------|
| 4 mm | 357.72 | 352.57 | 236,500 |
| 6 mm | 353.85 | 348.71 | 231,200 |
| 8 mm | 348.91 | 343.74 | 220,600 |

Broadening the straight channel can not only reduce the flow resistance, but also increase the heat exchange area so as to reduce the heat source temperature. However, widening the flow channel at the bend could promote the phenomenon of vapor separation, resulting in local dryness. Figure 10 shows the vapor-phase distribution at the bend of different channel sizes. For both channel sizes, when the two-phase flow passes through the bend, under the action of centrifugal force, the liquid tends to rush to the outside of the bend and the vapor is squeezed into the inside of the bend, resulting in the difference of vapor-phase distribution between the inside and outside of the bend. When the channel width is increased, the vapor separation at the bend is intensified, and the volume and diffusion area of the steam film inside the bend are significantly larger than those of the channel before widening, which will cause local dryness and lead to the occurrence of critical heat flux (CHF). This phenomenon should be avoided when considering engineering safety.

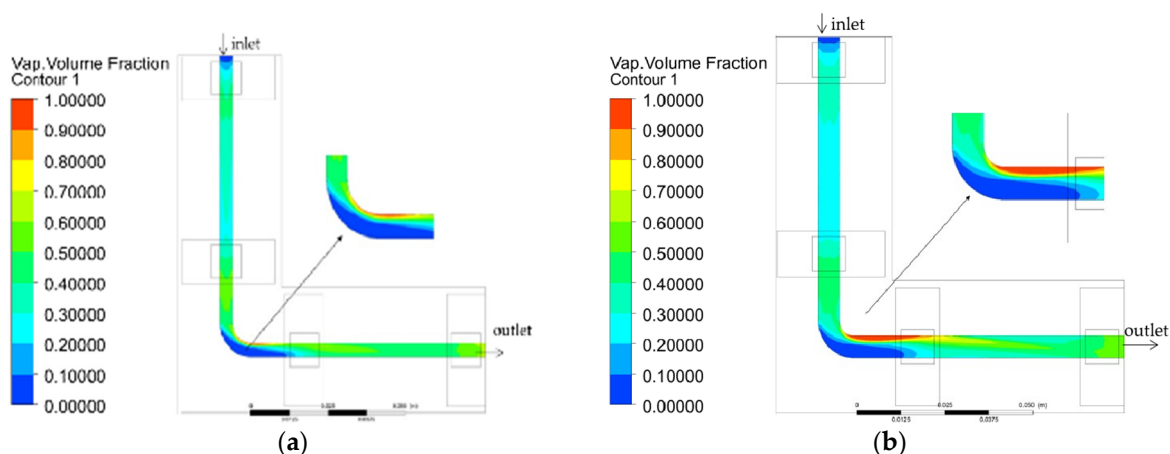


Figure 10. Vapor-phase distribution of different channel size; (a) 4 mm × 3 mm; (b) 6 mm × 3 mm.

3.4. Effect of the Relative Position of Heat Source and Curved Channel on Heat Transfer Performance and Pressure Drop Characteristics

Table 5 shows the numerical results of the highest temperature and average temperature of the heat source and pressure drop of the channel when the heat sources are located at different positions. Models 1–4 represent that the heat source is placed in front of the bend, near the bend, just above the bend and behind the bend, respectively. The heat transfer effect is the best when the heat source is near the bend, followed by the one behind the bend, and the worst is that in front of the bend.

Table 5. Numerical results of different heat source positions.

| Model | Highest Temperature of Heat Source/K | Average Temperature of Heat Source/K | Pressure Drop/Pa |
|-------|--------------------------------------|--------------------------------------|------------------|
| 1 | 371.30 | 369.28 | 978 |
| 2 | 368.18 | 366.13 | 851 |
| 3 | 370.50 | 368.16 | 928 |
| 4 | 369.49 | 367.46 | 787 |

Figure 11 shows the temperature distribution; it can be seen that the temperature is symmetrically distributed when the heat source is arranged at the straight channel (Figure 11a,d), while the temperature is higher on the outside and lower on the inside as the heat source is arranged just above the bend (Figure 11b,c). This is because the liquid flow rate outside the bend is slow and the heat dissipation effect is poor. This also explains that when the heat source is located just above the bend (model 3), although the area of the channel under the heat source is large, the temperature of the heat source is still high.

Figure 12 shows the vapor-phase distribution. It can be seen that when the heat source is set in front of the bend, the closer the heat source to the bend, the smaller the retention area of the liquid phase at the bend, and the less obvious the vapor–liquid separation, which indicates that the heat source can reform the vapor–liquid flow at the bend. Figure 12d shows that the downstream heater has little effect on the vapor fraction at the bend.

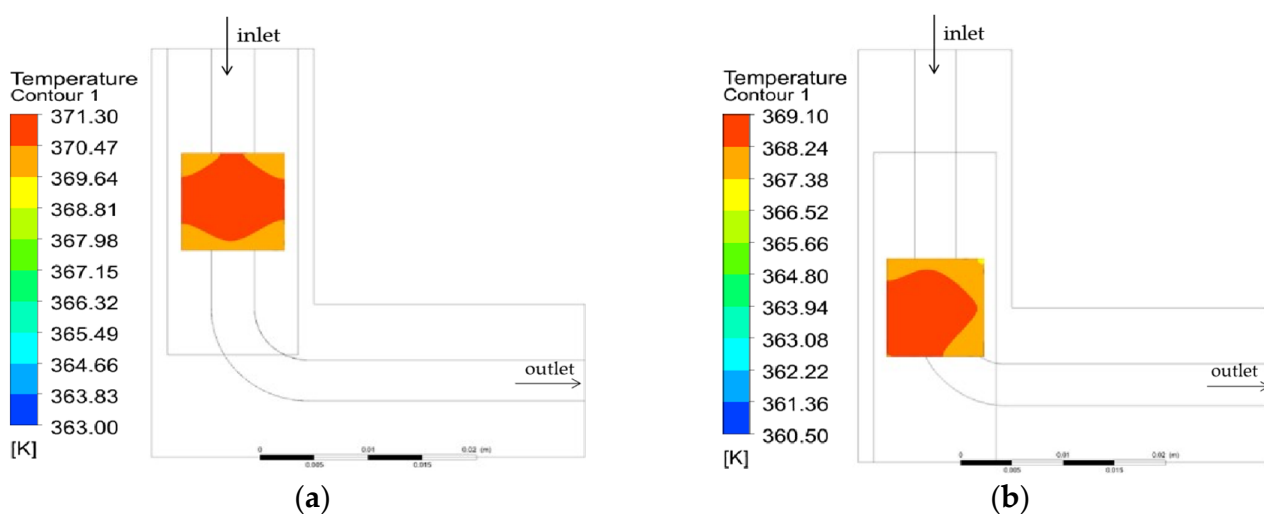


Figure 11. Cont.

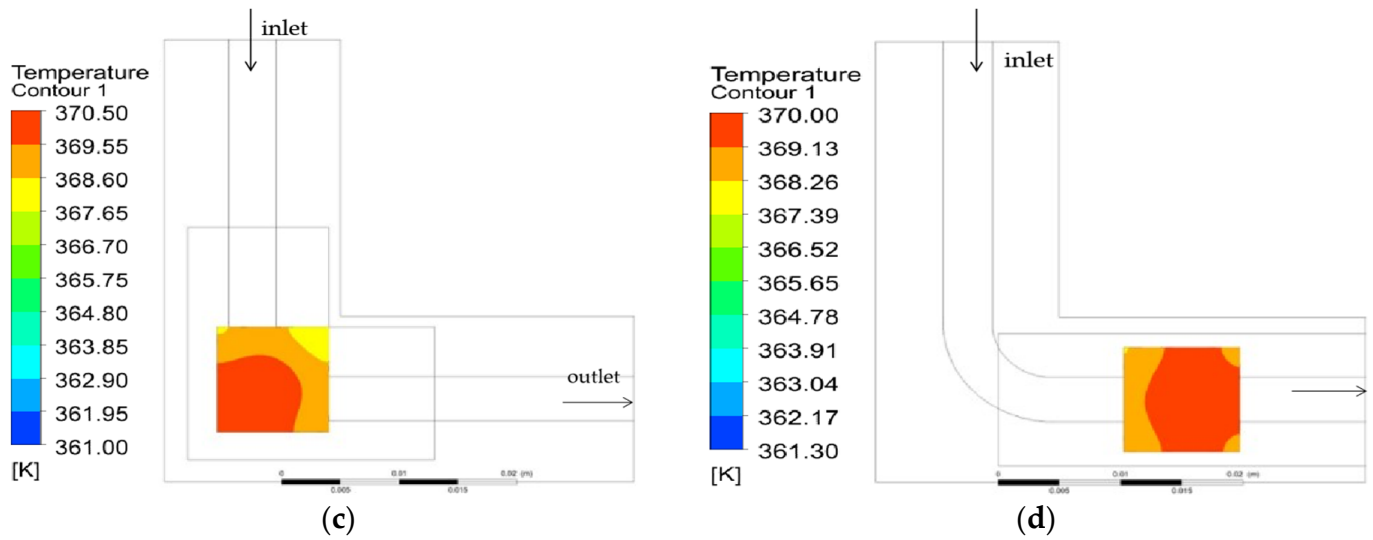


Figure 11. Temperature distribution when the heat source is set: (a) in front of the bend; (b) near the bend; (c) just above the bend; (d) behind the bend.

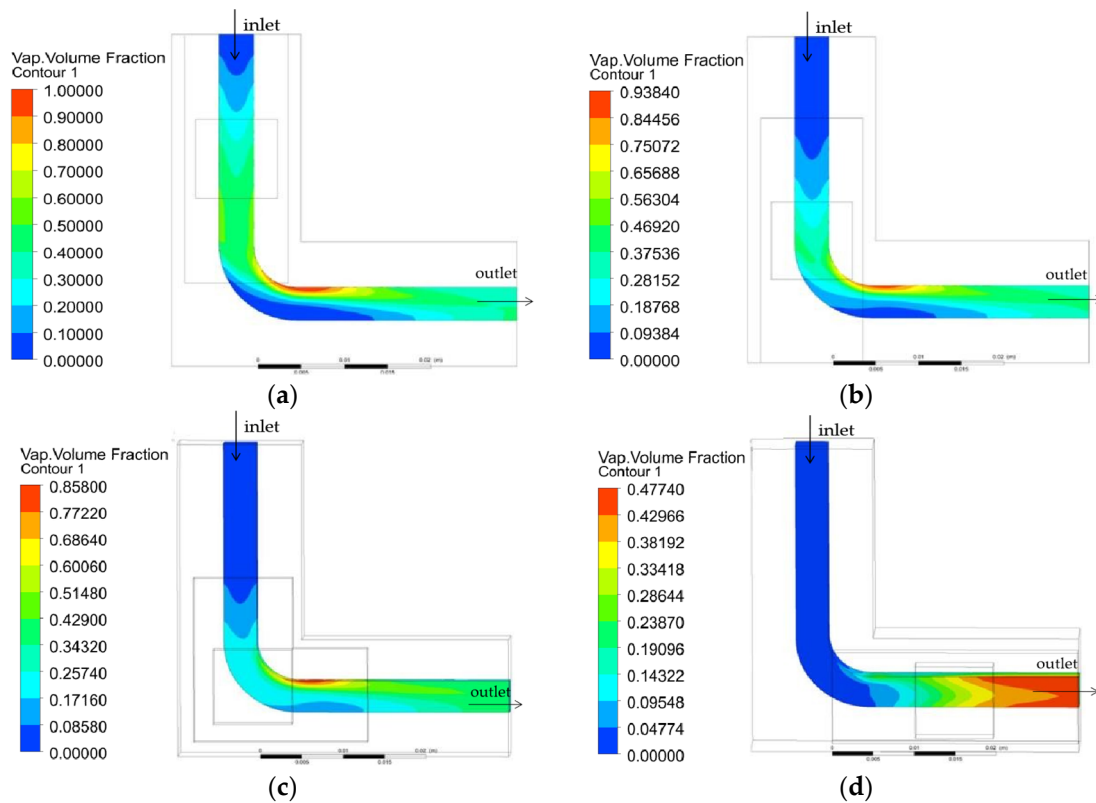


Figure 12. Vapor-phase distribution when the heat source is set: (a) in front of the bend; (b) near the bend; (c) just above the bend; (d) behind the bend.

3.5. Effect of the Bend Radius on Heat Transfer Performance and Pressure Drop Characteristics

The radius of the bend will change the centrifugal force of the fluid, as well as change the velocity, thus, influencing the heat transfer and fluid flow. Figure 13 shows the vapor-phase distribution of different bend radii, and the relevant numerical results are shown in Figure 14. The outside radius of the model bend is 5 mm, 7 mm, 9 mm, 11 mm, and 13 mm, respectively, and the inside radius is 4 mm smaller than the outside radius to control the

channel width. Two heat sources are located in front of the bend and behind the bend, respectively, for all the models.

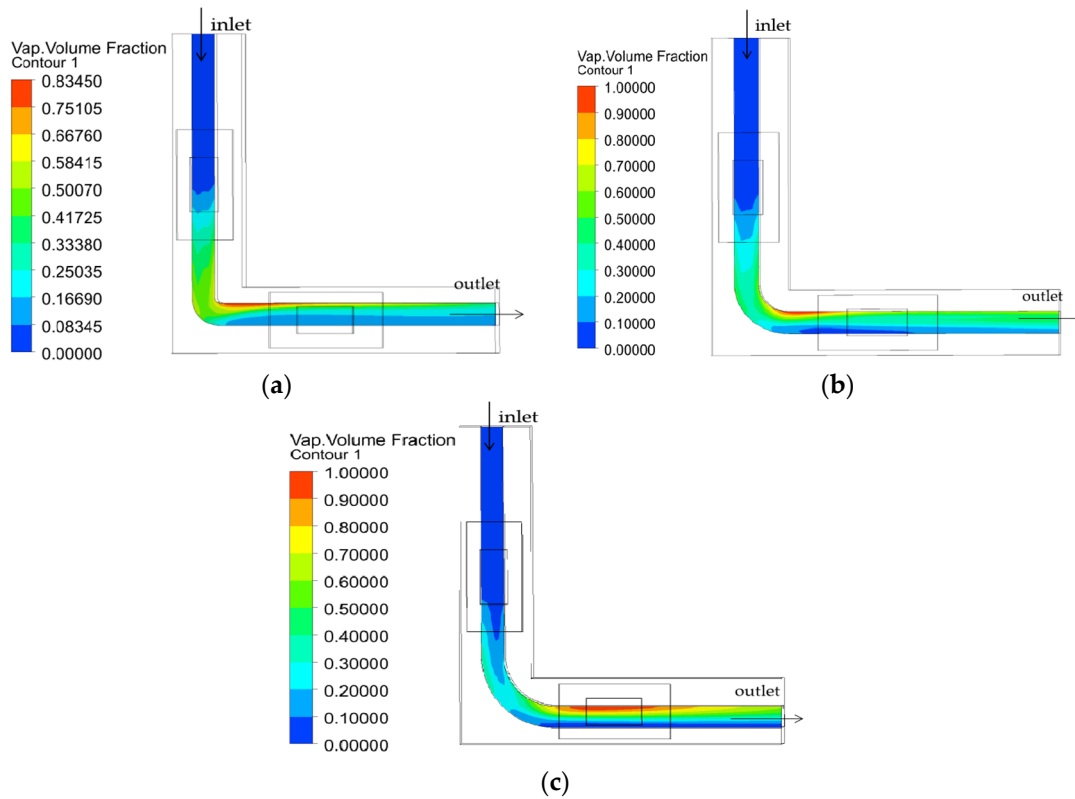


Figure 13. Vapor-phase distribution. The radius of each model is (a) 5 mm; (b) 9 mm; (c) 13 mm.

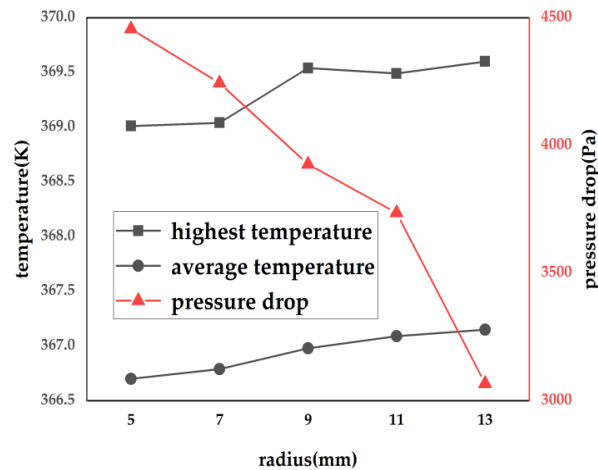


Figure 14. Change of the temperature and the pressure drop with radius.

Figure 13 shows that with the increase in the bend radius, the phenomenon of vapor-liquid separation becomes more obvious, and the vapor-phase and liquid-phase aggregation areas tend to extend. Figure 14 shows that with the increase in the radius outside the bend, the heat transfer effect worsens and the pressure drop in the channel decreases, which correlates with the local resistance calculation formula. This is because with the increase in the radius of the bend, the bend is smoother and the disturbance to the fluid decreases; thus, the boundary layer destruction weakens and the heat transfer effect worsens.

4. Conclusions

In this paper, the Eulerian method is used to establish a three-dimensional numerical calculation model of the cooling plate. The temperature of the heat source and the change of vapor distribution at the bend under different geometric parameters of the channel are discussed, and the effects of the position of the heat source on the flow boiling performance of the heat sink are studied. The main conclusions are as follows.

- (a) The temperature of the heat sources increases along the flow direction, but the heat sources in a continuous corner position are contrary to this trend. Vapor separation occurs at the corners.
- (b) A flat channel under the heat source can effectively reduce the heat source temperature due to the better-mixed flow and disturbance. With the increase in channel width, the temperature of the heat source decreases. Compared with the original channel, the 8 mm × 1.5 mm channel can reduce the temperature of the heat source by more than 2 K.
- (c) Broadening the straight channel can not only reduce the flow resistance, but also increase the heat exchange area and reduce the heat source temperature. However, widening the channel at the bend may enhance vapor–liquid separation, resulting in local dryness.
- (d) The relative position between the heat source and the bend can affect the heat dissipation effect and the vapor–liquid distribution at the bend. When the heat source is in front of the bend, the vapor–liquid separation is less obvious as it is closer to the bend, and the heat source located behind the bend has little effect on the vapor fraction at the bend. The heat transfer effect of the heat source near the bend is the best, followed by the one behind the bend, and the worst is that in front of the bend.
- (e) The radius of the bend affects the vapor–liquid distribution, heat transfer effect, and pressure drop. With the increase in the bend radius, the phenomenon of vapor separation becomes more obvious, the pressure drop of the pipeline decreases, but the heat transfer effect worsens.

Author Contributions: Conceptualization, D.H.; Methodology, J.Q.; Funding acquisition, J.Q.; Software, R.W.; Formal analysis, R.W. and T.W.; Investigation, J.Q.; Writing—original draft preparation, H.T.; Writing—review and editing, D.H., J.Q., R.W., T.W. and H.T. All authors have read and agreed to the published version of the manuscript.

Funding: This research was funded by the National Natural Science Foundation of China (No. 52276070), as well as by the Fundamental Research Funds for the Central Universities (No. 30922010903).

Institutional Review Board Statement: Not applicable.

Informed Consent Statement: Not applicable.

Data Availability Statement: Not applicable.

Acknowledgments: We would like to thank all contributors who supported the field work and the data collection and analysis.

Conflicts of Interest: The authors declare no conflict of interest.

References

1. Yao, S.G.; Ma, Z.S.; Luo, L. Research status and development of high-efficiency heat pipe technology in electronic and electrical equipment. *J. Jiangsu Univ. Sci. Technol. Nat. Sci. Ed.* **2003**, *17*, 9–12.
2. Xie, Y.C. Development of heat dissipation technology of electronic equipment. *Ship Electron. Eng.* **2019**, *1*, 39.
3. Wang, M.Y. *Research on the Topology Structure of Micro-Channel Cooling Plate of Active Phased Array Antenna*; University of Electronic Science and Technology of China: Chengdu, China, 2018.
4. Palm, B. Heat transfer in micro-channels. *Micro-Scale Therm. Phys. Eng.* **2001**, *5*, 155–175. [[CrossRef](#)]
5. Zhang, H.Y.; Pinjala, D.; Joshi, Y.K. Fluid flow and heat transfer in liquid cooled foam heat sinks for electronic packages. *IEEE Trans. Compon. Packag. Technol.* **2005**, *2*, 272–280. [[CrossRef](#)]
6. Cho, E.S. Experimental study on micro-channel heat sinks considering mass flow distribution with non-uniform heat flux conditions. *Int. J. Heat Mass Transf.* **2010**, *53*, 2159–2168. [[CrossRef](#)]

7. Kim, S.Y.; Hwang, K.; Moon, J.; Karng, S.W. Thermal management of liquid-cooled cooling plates for multiple heat sources in a humanoid robot. In Proceedings of the 4th Assembly and Circuits Technology Conference, Beijing, China, 21–23 October 2009.
8. Mao, Z.M.; Luo, X.B.; Liu, S. Compact thermal model for micro-channel substrate with high temperature uniformity subjected to multiple heat sources. In Proceedings of the 61st Electronic Components and Technology Conference, San Diego, CA, USA, 5 June 2011.
9. Ma, Z.T.; Wang, X.J.; Zhu, D.Q.; Liu, S. Thermal analysis and modeling of LED array integrated with an innovative liquid-cooling. In Proceedings of the IEEE 6th ICEPT, Shenzhen, China, 30 August–2 September 2005.
10. Yuan, L.L.; Liu, S.; Chen, M.X.; Luo, X.B. Thermal analysis of high power LED array packaging with micro-channel cooler. In Proceedings of the IEEE 7th ICEPT, Shanghai, China, 26–29 August 2006.
11. Tan, H. Topology design of micro-channel cooling plate of multi-heat source phased array antenna. *J. Univ. Electron. Sci. Technol. China* **2019**, *48*, 150–155.
12. Wei, T.; Huang, H.; Ma, Y.; Qian, J. Design and fabrication of multi-layer silicone micro-channel cooler for high-power chip array. In Proceedings of the 22nd International Conference on Electronic Packaging Technology, Xiamen, China, 14–17 September 2021; pp. 1–5.
13. Qian, S.; Wang, W.; Ge, C.; Lou, S.; Miao, E.; Tang, B. Topology optimization of fluid flow channel in cold plate for active phased array antenna. *Struct. Multidiscip.* **2017**, *57*, 2223–2232. [[CrossRef](#)]
14. Luo, X.; Mao, Z. Thermal modeling and design for micro-channel cold plate with high temperature uniformity subjected to multiple heat sources. *Int. Commun. Heat Mass* **2012**, *39*, 781–785. [[CrossRef](#)]
15. Drummond, K.P.; Back, D.; Sinanis, M.D.; Janes, D.B.; Peroulis, D.; Weibel, J.A.; Garimella, S.V. A hierarchical manifold micro-channel heat sink array for high-heat-flux two-phase cooling of electronics. *Int. J. Heat Mass Transf.* **2018**, *117*, 319–330. [[CrossRef](#)]
16. Tan, H.; Du, P.; Zong, K.; Meng, G.; Gao, X.; Li, Y. Investigation on the temperature distribution in the two-phase spider netted micro-channel network heat sink with nonuniform heat flux. *Int. J. Therm. Sci.* **2021**, *169*, 107079. [[CrossRef](#)]
17. Cong, B.; Kong, Y.; Ye, Y.; Liu, R.; Du, X.; Yu, L.; Jia, S.; Jiao, B.; Qu, Z. A combined solution of thermoelectric coolers and micro-channels for multi-chip heat dissipation with precise temperature uniformity control. *Appl. Therm. Eng.* **2022**, *219*, 119370. [[CrossRef](#)]
18. Laguna, G.; Vilarrubí, M.; Ibañez, M.; Betancourt, Y.; Illa, J.; Azarkish, H.; Amnache, A.; Collin, L.M.; Coudrain, P.; Fréchette, L.; et al. Numerical parametric study of a hotspot-targeted microfluidic cooling array for microelectronics. *Appl. Therm. Eng.* **2018**, *144*, 71–80. [[CrossRef](#)]
19. Li, X.; Xuan, Y.; Li, Q. Self-adaptive chip cooling with template-fabricated nanocomposite P(MEO2MA-co-OEGMA) hydrogel. *Int. J. Heat Mass Transf.* **2021**, *166*, 120790. [[CrossRef](#)]
20. Yu, Z.; Yuan, H.; Chen, C. Two-phase flow instabilities of forced circulation at low pressure in a rectangular mini-channel. *Int. J. Heat Mass Transf.* **2016**, *98*, 438–447. [[CrossRef](#)]
21. Zhang, X.; Yu, T.; Cong, T.; Peng, M. Effects of interaction models on upward subcooled boiling flow in annulus. *Prog. Nucl. Energy* **2018**, *105*, 61–75. [[CrossRef](#)]
22. Krepper, E.; Rzehak, R.; Lifante, C.; Frank, T. CFD for subcooled flow boiling: Coupling wall boiling and population balance models. *Nucl. Eng.* **2013**, *255*, 330–346. [[CrossRef](#)]
23. Cole, R. A photographic study of pool boiling in the region of the critical heat flux. *AIChE J.* **1960**, *6*, 533–542. [[CrossRef](#)]
24. Dai, N. *Experimental Study on Flow Characteristics of Gas-Liquid Two-Phase Flow in a Serpentine Tube*; Shandong University: Jinan, China, 2021.

Disclaimer/Publisher’s Note: The statements, opinions and data contained in all publications are solely those of the individual author(s) and contributor(s) and not of MDPI and/or the editor(s). MDPI and/or the editor(s) disclaim responsibility for any injury to people or property resulting from any ideas, methods, instructions or products referred to in the content.